PCCP
Physical Chemistry Chemical Physics

This article can be cited before page numbers have been issued, to do this please use: Y. Yang, Q. Huang, J. Kuo and A. Fujii, *Phys. Chem. Chem. Phys.*, 2026, DOI: 10.1039/D6CP00987E.

Volume 19
Number 1
7 January 2017
Pages 1-896

PCCP
Physical Chemistry Chemical Physics
rsc.li/pccp

ISSN 1463-9076

ROYAL SOCIETY OF CHEMISTRY

PAPER
H.-P. Loock *et al.*
Determination of the thermal, oxidative and photochemical degradation rates of scintillator liquid by fluorescence EEM spectroscopy

ROYAL SOCIETY
OF CHEMISTRY

rsc.li/pccp

View Article Online
DOI: 10.1039/D6CP00987E

Near infrared spectroscopy of micro-solvated protonated methanol

Yaodi Yang,[†,a] Qian-Rui Huang,[†,b] Jer-Lai Kuo,*[b] and Asuka Fujii*[a]

[a] *Department of Chemistry, Graduate School of Science, Tohoku University, Sendai, Japan.*

[b] *Institute of Atomic and Molecular Sciences, Academia Sinica, Taipei, Taiwan.*

Email: jlkuo@pub.iams.sinica.edu.tw (J. -L. K), asuka.fujii.c5@tohoku.ac.jp (A.F.)

† These authors contributed equally to this work.

Abstract

Gas phase near-infrared (NIR) spectra of micro-solvated protonated methanol, $MeOH_2^+\cdots X_n$ (X = Ar, N_2, and CO; n = 1 and 2), in the region of the first overtones of OH stretches were obtained via infrared photodissociation spectroscopy. Spectral details were analyzed with the support of high-precision *ab initio* anharmonic simulations. The free OH stretching overtones and combination bands of OH stretch and bend are the main features in this region. The hydrogen-bonded OH stretching overtone transitions exhibit weak and broad characteristics across all solvents (X). This trend increases with the proton affinity of X. Hot bands, intramolecular vibrational energy redistribution, and band congestion due to strong anharmonic couplings are proposed to have played crucial roles in this observation. Meanwhile, perturbations from low frequency modes, such as CH/OH rocking, CH bending, and solvent intramolecular vibrations, should not be overlooked in this cluster system. Our anharmonic algorithm has demonstrated its potential in reproducing precise NIR spectra, and the present system can serve as a benchmark for theoretical anharmonic computations in the NIR region.

View Article Online
DOI: 10.1039/D6CP00987E

Introduction

Near-infrared (NIR) spectroscopy, which directly probes higher vibrational levels, provides valuable and unique information on phenomena such as anharmonic couplings, the shape of the potential energy surface, and intramolecular vibrational energy redistribution (IVR).[1–8] Gas phase molecular clusters, on the other hand, are well-defined systems that are highly useful for fundamental modeling of complex systems.[9] Charged clusters can be readily size-selected by mass spectrometry and are often combined with infrared (IR) spectroscopy to investigate their geometric and vibrational structures.[9] However, applying NIR spectroscopy to size-selected gas phase clusters has been very limited. This is primarily due to the extremely weak transition intensities in this region.

Furthermore, combination bands (CBs), overtones, and other vibrational couplings that arise from anharmonicities of clusters present additional challenges for spectral interpretation in the NIR region. Experimental vibrational spectra of gas phase clusters serve as direct benchmarks for high-precision computational chemistry, which in turn provides theoretical basis for elucidating observed spectral features. Although the theoretical modeling of NIR spectra can be traced back to the mid-twentieth century,[10] reliable and in-depth analyses only become possible with the advent of high-precision anharmonic vibrational methods. Despite these advancements, reproducing NIR spectra still demands significant computational efforts, even for very simple molecular systems.

Recent advances in anharmonic vibrational approaches have enabled qualitative and even quantitative anharmonic analyses of small-sized protonated systems, such as protonated water, ammonia, alcohol, and amine clusters in the mid-infrared (MIR) region.[11–31] These protonated hydrogen-bonded (H-bonded) systems have long been one of the major topics in gas phase vibrational spectroscopy, owing to the ubiquity and

View Article Online
DOI: 10.1039/D6CP00987E

significance of proton solvation and the need for its microscopic understanding.

There have also been some efforts on NIR spectroscopy of protonated and/or neutral H-bonded species in the gas phase, including trials to verify the compatibility of anharmonic algorithms in the NIR region.[32–39] McDonald *et al.* reported the NIR spectra of protonated water clusters, $H^+(H_2O)_n$ ($n = 4 - 8$), and Ar-tagged protonated water clusters, $H^+(H_2O)_n \cdots Ar$ ($n = 1 - 4$), using infrared photodissociation (IRPD) spectroscopy in the frequency range of 3600 – 7300 cm^{-1}.[35] While the first overtones of the Ar-bound OH stretches were clearly visible in the Ar-tagged water clusters, overtones of the water-bound OH stretches were either very weak or entirely absent. In the case of protonated water dimer, the water-bound OH stretching overtone is expected to show an exceptionally low frequency transition owing to its symmetrically shared proton structure, making it understandably difficult to detect.[40,41] However, such transitions of the clusters with $n > 2$ were still expected to be observed in the region probed by McDonald *et al.* From a micro-solvation perspective, the H_2O molecules and the Ar messenger act as solvents filling the first solvation shell of the central H_3O^+. Since H_2O is a much stronger proton acceptor compared to Ar, the effect of tuning the solvation environment on the OH stretching overtones of the solvated cation has emerged as a focal point for us.

Previously, we measured the NIR spectra of micro-solvated protonated water clusters, $H_3O^+ \cdots X_n$ (X = Ar, N_2 and CO; $n = 1 - 3$) by IRPD spectroscopy.[37] Detailed spectral features were analyzed with the guidance of high-precision anharmonic vibrational calculations.[37] The observed spectra of these clusters broadened significantly as proton affinity (PA) of the binding solvent increased (with PA following the order $Ar < N_2 < CO < H_2O$), regardless of the cluster size (n).

To test the generality of these findings, we plan to shift our focus to protonated

View Article Online
DOI: 10.1039/D6CP00987E

methanol ($MeOH_2^+$). As an analog to the protonated water system, the spectra of protonated methanol are expected to show similar spectral patterns under the similar solvation environment. However, there are some key differences. The presence of only two OH bonds in a protonated methanol should, in principle, make its spectrum less complex compared to protonated water, which can act as a proton donor to form up to three OH···X H-bonds with surrounding solvent species. On the other hand, based on our previous work with MIR spectra of micro-solvated clusters of protonated methanol and protonated methylamine,[27,31] the methyl group on $MeOH_2^+$ is expected to cause a non-negligible perturbation to the spectrum through the methyl-hydroxyl rocking motions.

In this work, we continue to use the same solvent species (X = Ar, N_2 and CO) that were used for our previous study on the $H_3O^+\cdots X_n$ clusters. By varying the solvent species and the number of binding solvents (n = 1 and 2), we aim to evaluate the capability of our *ab initio* anharmonic algorithm for overtone analyses and to uncover the anharmonic coupling patterns in the NIR region of the $MeOH_2^{+}\cdots X_n$ clusters.

Experimental setup

The protonated methanol clusters were produced by the collision of an electron beam with a pulsed supersonic jet expansion of a gaseous mixture containing methanol, solvent X (X = Ar, N_2 and CO), and carrier gas (Ar or He). An Even-Lavie pulsed valve,[42] operating at a stagnation pressure of 80 atm, was used for the jet expansion. Such a high operating pressure facilitates more collisions, which ensures effective cooling of the weakly-bound clusters. Parent ions ($MeOH_2^{+}\cdots X_n$) were mass-selected by the first quadrupole mass analyzer of a tandem type mass spectrometer. Subsequently, they were transferred into an octupole ion guide, in which vibrational predissociation occurred following exposure

View Article Online
DOI: 10.1039/D6CP00987E

to a pulsed beam of tunable NIR light. The NIR light source used in this work was the output of an Nd:YAG laser (Spectra Physics GGR230) pumped IR-OPO/OPA (LaserVision). The resulting fragment ions ($MeOH_2^{+}\cdots X_{n\text{-}1 \text{ or } n\text{-}2}$), which had lost one or two solvent molecules, were selected at the second quadrupole mass analyzer before being detected by an ion detector at the end of the mass-spectrometer. The signal difference of the fragment ions, measured with and without irradiation of the NIR light was monitored, power-normalized, and plotted against scanned frequency for the dissociation spectrum. A more detailed description of the experimental setups can be found elsewhere.[43]

Computational details

Geometric structures of the protonated methanol clusters, $MeOH_2^{+}\cdots X_n$ (X = Ar, N_2 and CO), were optimized at the MP2/aug-cc-pVDZ level using Gaussian 16.[44] Cartesian coordinates of the optimized structures are provided in **Table S1** of the Supplementary Information (SI). The number of plausible isomers for small-sized clusters is limited. Only one low energy isomer was found for each individual cluster in this work, where each OH bond is solvated by a single solvent molecule. Other isomers, *e.g.*, those in which a solvent molecule dimer is bound to one of the OH bonds, are much higher in energy, and their contribution to the NIR region is negligible.

All vibrational calculations were carried out at the MP2/aug-cc-pVDZ equilibrium geometry. The partial Hessian vibrational analysis (PHVA) was used to obtain localized normal modes (LNM) for reduced-dimensional vibrational analysis.[45] These LNMs provide a fragment-focused representation of the vibrational motions which allows us to isolate the most relevant motions for high-level anharmonic analysis. The applicability of

View Article Online
DOI: 10.1039/D6CP00987E

this approach has been demonstrated in our previous studies, including the analysis of the MIR spectra of $MeOH_2{}^+\cdots X$□.[31,46,47] Here, the same strategy is adopted. The LNMs used in this work are summarized in **Table S2**.

A subset of vibrational modes was selected to explicitly describe the NIR spectral region of interest. These include 2 OH stretching modes (s), 1 HOH bending mode (b), 1 or 2 intermolecular stretching modes (t), 4 CH/OH rocking motions (R), and, when applicable, the intramolecular stretching modes (s_X) of the solvent molecule ($N\equiv N$ or $C\equiv O$). The selected localized normal modes of $MeOH_2{}^+\cdots N_2$ used in the calculations are visualized in **Figure S1** as examples. Each selected normal mode was represented using discrete variable representation (DVR) based on Gauss–Hermite quadrature.[48,49] Seven grid points were employed for each mode coordinate. This choice was motivated by previous convergence tests on protonated water clusters.[37] It was demonstrated that this grid size provides sufficient accuracy for describing anharmonic vibrational features in the NIR region.

A direct-product DVR grid for the full-dimensional system would formally contain up to $7^{11} \approx 2 \times 10^9$ grid points, which would make direct diagonalization infeasible. This led to the application of *n*-mode representation (*n*MR) to the PES, followed by a transformation into finite basis representation (FBR) and subsequent truncation into a smaller Hamiltonian. The PES was expanded using the *n*MR scheme proposed by Carter *et al.*[50] as follows

$$V(q_i,q_j,q_k,\ldots) = V^{(0)} + \sum_i \Delta V_i^{(1)}(q_i) + \sum_{ij} \Delta V_{ij}^{(2)}(q_i,q_j)$$
$$+ \sum_{ijk} \Delta V_{ijk}^{(3)}(q_i,q_j,q_k) + \sum_{ijkl} \Delta V_{ijkl}^{(4)}(q_i,q_j,q_k,q_l) + \ldots$$

View Article Online
DOI: 10.1039/D6CP00987E

where $V^{(0)}$ is the energy at the equilibrium geometry, and $\Delta V_{\{i\}}^{(n)}$ terms describe n-mode coupling contributions from modes $\{i\}$. In this work, the expansion was truncated at the four-mode level (4MR). The most essential terms, $V^{(0)}$ to $\Delta V_{ij}^{(2)}$, were calculated at the DLPNO-CCSD(T)/def2-QZVPPD level for better precision. As higher-order coupling terms contribute less significantly to the total PES, three- and four-mode couplings terms, $\Delta V_{ijk}^{(3)}$ and $\Delta V_{ijkl}^{(4)}$, were evaluated at the RI-MP2/def2-QZVPPD level. The dipole moment surface was constructed using an *n*-mode expansion analogous to that employed for the PES. All electronic structure calculations for PES scans were performed with ORCA 6.0.0.[51]

To enable efficient diagonalization for up to 11 explicitly treated modes, we employed a finite-basis representation (FBR) built from eigenfunctions of the one-dimensional single-mode DVR Hamiltonians.[48] For each selected normal coordinate q_i, the corresponding 1D Hamiltonian, $\hat{H}_i = \hat{T}_i + V_i^{(1)}$, was represented on a Gauss–Hermite DVR grid, and diagonalized to obtain a set of single-mode eigenfunctions, $\{\phi_{n_i}(q_i)\}$. The multi-dimensional vibrational basis functions were then expressed as direct products $|n\rangle = \prod_i \phi_{n_i}(q_i)$. Rather than using the full direct-product basis, a configuration-selected basis was employed using two filters:

1. **VCI-type total-quanta truncation**: only configurations satisfying $\sum_i n_i \leq Q_{\max}$ were retained. In this work, $Q_{\max} = 7$ or 8 was used to balance accuracy and computational cost. Production calculations employed $Q_{\max} = 7$ to enable an efficient projection of eigenvectors onto another FBR basis built from products of selected *n*-dimensional eigenfunctions. Convergence was assessed by repeating representative calculations with $Q_{\max} = 8$ with the primitive basis (see **Figure S2** in the SI).

View Article Online
DOI: 10.1039/D6CP00987E

2. **Energy-window truncation**: Each product basis function $|n\rangle$ was assigned an approximate energy, $E_{\mathrm{n}}^{\mathrm{est}} = \sum_i \varepsilon_{n_i}$, where ε_{n_i} is the eigenvalue of the 1D eigenfunction ϕ_{n_i}. Only configurations with $E_{\mathrm{n}}^{\mathrm{est}} \leq$ 25000 cm^{-1} were included in the final FBR basis.

Off-diagonal Hamiltonian couplings $\langle a \,|\, \hat{H} \,|\, b \rangle$ were also neglected when both basis functions $|a\rangle$ and $|b\rangle$ have estimated energies in the interval 20000-25000 cm^{-1}. This screening affects only couplings among highly excited configurations well above the targeted spectral range (0-8000 cm^{-1}). Diagonal elements were retained for all selected basis functions.

The 4MR PES enables the Hamiltonian matrix elements in the FBR basis to be evaluated using low-dimensional integrals. Specifically, for each *n*-mode coupling term $\Delta V_{\{i\}}^{(n)}$, we evaluated the corresponding matrix elements in the product basis of the involved modes, $\left\langle \{i_a\} \,\middle|\, \Delta V_{\{i\}}^{(n)} \,\middle|\, \{i_b\} \right\rangle$. These low-dimensional blocks were generated once and reused. The full-dimensional Hamiltonian elements, $\langle a \,|\, \hat{H} \,|\, b \rangle$, were assembled by combining contributions from the relevant *n*-mode potential blocks, exploiting the fact that each *n*-mode term only couples a limited subset of quantum indices. This strategy avoids explicit construction of the full direct-product Hamiltonian on the DVR grid and substantially reduces the computational cost. Meanwhile, the matrix-element generation and assembly were embarrassingly parallelized over multiple CPU cores.

The resulting sparse Hamiltonian was solved using Extended Eigensolver in Intel MKL, which is based on Krylov–Schur algorithm.[52,53] Eigenpairs were computed for states up to 8000 cm^{-1} above the vibrational ground state. No empirical scaling factors were applied to the calculated vibrational frequencies. Simulated spectra were obtained by applying Lorentzian broadening with a full width at half maximum (FWHM) of 10

View Article Online
DOI: 10.1039/D6CP00987E

cm^{-1}.

Results and discussion

The IRPD spectra for both the singly and doubly solvated protonated methanol clusters were measured in the first overtone region of the OH stretching modes (4700 – 7200 cm^{-1}). Additionally, spectra in the frequency range of 3800 – 4700 cm^{-1} were also obtained primarily to assist with band assignments. In practice, an inevitable gap (<20 cm^{-1}) exists between these two frequency ranges due to the photon splitting process of OPA. Consequently, the absolute intensity ratios of observed IR signals from the two distinct frequency ranges cannot be determined.

Singly solvated protonated methanol MeOH$_2^+$···X

The observed NIR spectra of the singly Ar-solvated protonated methanol, MeOH$_2^+$···Ar, is shown by the black trace in **Figure 1a**. The signal intensity of the photodissociation fragment ions was about two orders of magnitude weaker than that observed in the OH stretching fundamental region. Hence, extensive spectrum accumulation (over 10 scans) was required to improve the signal-to-noise (S/N) ratio of the observed spectrum. The sharp band at the high energy end of the spectrum (6948 cm^{-1}) is assigned to the first overtone transition of the free OH stretching vibration, $|s_{\mathrm{free}}^2\rangle$. Its fundamental transition was previously found at 3555 cm^{-1} in our study of the MIR spectra of MeOH$_2^+$···X$_n$.[31] The most intense band in the observed spectrum appears at 5170 cm^{-1}. This frequency region is consistent with the CB of one quantum HOH bend (transition at ~1600 cm^{-1}) and one quantum free OH stretch, $|b + s_{\mathrm{free}}\rangle$. While the strongest transition in the MIR region is the Ar-bound (H-bonded) OH stretch (~3300 cm^{-1}), its overtone transition, $|s_{\mathrm{HB}}^2\rangle$, peaking around 6430 cm^{-1}, is significantly weaker than either $|s_{\mathrm{free}}^2\rangle$ or the major CB of $|b + s_{\mathrm{free}}\rangle$. Such a profound suppression of the $|s_{\mathrm{HB}}^2\rangle$ transition was not clearly

View Article Online
DOI: 10.1039/D6CP00987E

observed in the micro-solvated hydronium ion clusters until solvation by CO,[37] though similar suppressions have been generally reported in condensed phase studies of H-bonded species.[32,54–59] Despite this, the gross feature of the observed NIR spectrum of $MeOH_2^+\cdots Ar$ basically resembles that of $H_3O^+\cdots Ar$.[35,37]

The simulated DVR-FBR spectrum of $MeOH_2^+\cdots Ar$ (red trace in **Figure 1a**) is in overall good agreement with the observed spectrum. A few minor experimental features are not reproduced, most notably near 6000 cm^{-1}, where overtones and combination bands involving CH_3 bending and/or stretching vibrations are expected. These transitions are not captured in the present reduced-dimensionality vibrational analysis because the corresponding CH_3 modes were not included explicitly in the DVR–FBR treatment. Their harmonic fundamentals are listed in **Table S2** for reference. According to the assignment table for pronounced calculated transitions (**Table S3**), the assignments based on the simulation are consistent with the qualitative interpretation given above. The relatively weaker band at 6875 cm^{-1} next to $|s_{\mathrm{free}}^2\rangle$ can be attributed to the CB of $|s_{\mathrm{free}}+s_{\mathrm{HB}}\rangle$. The structured band patterns in the lower frequency region (3800 – 5000 cm^{-1}) primarily result from combinations of the CH/OH rocking modes R with s_{free} or s_{HB}. A typical example is the $|R+s_{\mathrm{free}}\rangle$ peak centered at 4812 cm^{-1}, which also carries an intensity comparable to the $|s_{\mathrm{free}}^2\rangle$ transition.

Figure 1b displays the observed and calculated NIR spectra of $MeOH_2^+\cdots N_2$. The $|s_{\mathrm{free}}^2\rangle$ transition appears at 6960 cm^{-1}, and the dominant CB of $|b+s_{\mathrm{free}}\rangle$ is observed at 5196 cm^{-1}. These features exhibit only slight blueshifts relative to $MeOH_2^+\cdots Ar$. The overtone of N_2-bound OH stretching band, $|s_{\mathrm{HB}}^2\rangle$, centered at 5810 cm^{-1} (the corresponding fundamental was found at ~3100 cm^{-1})[31] is red-shifted by ~600 cm^{-1} relative to $|s_{\mathrm{HB}}^2\rangle$ in $MeOH_2^+\cdots Ar$. This pronounced redshift reflects a weakening of the

View Article Online
DOI: 10.1039/D6CP00987E

OH covalent bond due to the strengthened OH⋯N_2 H-bond. Consequently, the CB $|s_{\mathrm{free}} + s_{\mathrm{HB}}\rangle$ also shifts to 6640 cm^{-1}. In contrast, the $|s_{\mathrm{free}}^2\rangle$ band is hardly affected by the change of solvent species.

One of the most intriguing observations for $\mathrm{MeOH_2}^+\cdots\mathrm{N_2}$ is the relatively broad and weak appearance of the $|s_{\mathrm{HB}}^2\rangle$ transitions. The DVR-FBR calculation suggests that $|s_{\mathrm{HB}}^2\rangle$ is strongly mixed with nearby vibrational states, leading to pronounced spectral congestion. In the observed spectrum of $\mathrm{MeOH_2}^+\cdots\mathrm{N_2}$, there are a few resolvable minor peaks surrounding $|s_{\mathrm{HB}}^2\rangle$ at 5810 cm^{-1}. According to **Table S3**, the main intensity carriers of these bands originate from $|s_{\mathrm{HB}}^2\rangle$, which strongly mixes with other states such as $|s_{\mathrm{HB}}^2 + t\rangle$, $|R^2 + b^2\rangle$, and so on. This mixing results in intensity borrowing from the bright state $|s_{\mathrm{HB}}^2\rangle$ to various dark states, primarily through mechanical anharmonicity. The deep involvement of the R modes again highlights the contribution of the methyl group in the NIR region of protonated methanol clusters. In contrast, the $|s_{\mathrm{free}}^2\rangle$ transition of $\mathrm{MeOH_2}^+\cdots\mathrm{N_2}$ remains sharp, and its projection shows that it is almost free from couplings. Meanwhile, several weaker bands under the $|s_{\mathrm{HB}}^2\rangle$ envelope show nearly negligible contribution from $|s_{\mathrm{HB}}^2\rangle$. Their presence adds another layer of complexity to the assignment of the OH stretching overtone features.

An analogous situation occurs for the broad feature centered at ~5000 cm^{-1} in the spectrum of $\mathrm{MeOH_2}^+\cdots\mathrm{Ar}$ in **Figure 1a**, which lies between the $|b + s_{\mathrm{free}}\rangle$ and $|R + s_{\mathrm{free}}\rangle$ peaks. This feature is loosely attributed to the CB $|b + s_{\mathrm{HB}}\rangle$. However, a more careful review of its composition reveals that similar state mixing effects, including Fermi resonance (FR)-like interactions between the $|b + s_{\mathrm{HB}}\rangle$ state and $|R^2 + s_{\mathrm{HB}}\rangle$ or $|R^2 + s_{\mathrm{HB}} + t\rangle$, have manifested themselves. These interactions appear in the form of intensity suppression of the main $|b + s_{\mathrm{HB}}\rangle$ transition and a broadened lineshape. Upon

View Article Online
DOI: 10.1039/D6CP00987E

replacing Ar with N_2, the $|s_{\mathrm{HB}}\rangle$ band shifts away from $|s_{\mathrm{free}}\rangle$, giving rise to a wider gap between $|s^2_{\mathrm{HB}}\rangle$ and $|s^2_{\mathrm{free}}\rangle$. The CB of $|b+s_{\mathrm{HB}}\rangle$ is expected to shift accordingly to ~4700 cm^{-1}, which unfortunately falls into the gap separating the two experimental scan ranges.

Figure 1c shows the observed and calculated spectra of $MeOH_2^+\cdots CO$. The $|s^2_{\mathrm{free}}\rangle$ band slightly blueshifts to 6972 cm^{-1}, and the intense feature at 5200 cm^{-1} can be assigned to the CB $|b+s_{\mathrm{free}}\rangle$. The CB $|R+s_{\mathrm{free}}\rangle$ appears at 4835 cm^{-1}. These bands remain essentially unshifted. However, assigning the CO-bound OH stretching overtone ($|s^2_{\mathrm{HB}}\rangle$) is not straightforward without the guidance from theoretical simulations. Given that CO has a larger PA than N_2,[60] the $|s^2_{\mathrm{HB}}\rangle$ band is expected to exhibit an additional redshift and it is therefore likely buried under the broad feature in the $4800-5200$ cm^{-1} region (its fundamental transition was found at ~2600 cm^{-1}).[31] The simulation (**Table S3**) indicates that $|s^2_{\mathrm{HB}}\rangle$ couples with many dark overtone/combination bands, but most of the projections of $|s^2_{\mathrm{HB}}\rangle$ are very low (less than 5%) in each case. In the lower frequency part, two groups of weak peaks around ~4200 cm^{-1} and ~4400 cm^{-1} are assigned as the CB $|b+s_{\mathrm{HB}}\rangle$, showing reasonable correspondence with the broad feature in the experimental spectrum.

Doubly solvated protonated methanol $MeOH_2^+\cdots(X)_2$

Figure 2 shows the observed and calculated NIR spectra of $MeOH_2^+\cdots(X)_2$. In the case of the singly solvated clusters, the free OH stretching overtones serve as intensity metrics due to their less perturbed character. However, these transitions are absent in the $n = 2$ spectra because both OH groups are solvated. Consequently, directly comparing the IR absorption intensities of the H-bonded OH stretching overtones across different solvent species is more challenging.

View Article Online
DOI: 10.1039/D6CP00987E

For $MeOH_2^+\cdots(Ar)_2$ (**Figure 2a**), the features observed at 6497 cm^{-1} and 6662 cm^{-1} are assigned to the first overtones of the Ar-bound OH stretches, $|s^2\rangle$. Both bands exhibit slight blueshifts relative to the $|s_{\mathrm{HB}}^2\rangle$ transition in $MeOH_2^+\cdots Ar$. This observation demonstrates the anti-cooperative effect of H-bonds,[61] in which the positive charge is delocalized to both proton acceptors during the formation of the second H-bond. This delocalization weakens the first H-bond and, in turn, strengthens the corresponding OH bond, which leads to an increase in its stretching frequency. **Table S3** further indicates that the OH stretching overtones are strongly coupled with nearby vibrational states. The intense feature at 5002 cm^{-1} is likely a CB of one-quanta OH bending and one-quanta OH stretching mode, $|b+s\rangle$.

The black trace in **Figure 2b** displays the experimental NIR spectrum of $MeOH_2^+\cdots(N_2)_2$ measured by monitoring the single N_2-loss channel, while the inset presents the spectrum obtained by monitoring the $2N_2$-loss channel. For photon energy above ~6000 cm^{-1}, absorption provides sufficient energy to trigger a switch in the major dissociation channel, which explains the absence of the OH stretching overtone bands in the single N_2-loss channel spectrum. Accordingly, the bands centered at 6090 and 6320 cm^{-1} in the inset are assigned to the N_2-bound $|s^2\rangle$ transitions. In the calculations, these bands are associated with many CBs. These overtone frequencies are redshifted by about 300 — 400 cm^{-1} compared to those of $MeOH_2^+\cdots(Ar)_2$. The CB of $|b+s\rangle$ is found at 4860 cm^{-1}, and is broader than the corresponding band in the spectrum of $MeOH_2^+\cdots(Ar)_2$. Our calculation suggests that it is engaged in couplings with the $|R+s\rangle$ and $|R+b^2\rangle$ states. The origin of the doublet at 5550 cm^{-1} is assigned to the CBs involving one-quanta N≡N stretching modes (s_{X}) and one-quanta H-bonded OH stretching modes, $|s+s_{\mathrm{X}}\rangle$.

Figure 2c presents the NIR spectrum of $MeOH_2^+\cdots(CO)_2$, in which pronounced

View Article Online
DOI: 10.1039/D6CP00987E

bands are concentrated in the 5000 ─ 6000 cm^{-1} region with a maximum at ~5200 cm^{-1}, which is attributed to overtones or CB of H-bonded OH stretches. The observed bands are substantially broadened, with linewidths in the order of a few hundred wavenumbers. The DVR-FBR simulation noticeably overestimated the major band position ($|s^2\rangle$) to ~5423 cm^{-1} in this case. To evaluate whether this discrepancy can be attributed to hot bands, we carried out a hot band simulation by initiating transitions from an excited H-bond stretching mode t, which has the lowest excitation energy among the vibrational modes included in our reduced-dimensional analysis and is therefore most thermally populated. The resulting simulated hot band spectra is shown in **Figure S3**. For the case of $MeOH_2^+\cdots(CO)_2$ (**Figure S3b**), the simulated transitions from $|t^1_{\mathrm{A''}}\rangle$ and $|t^1_{\mathrm{A'}}\rangle$ show intense bands at ~5320 cm^{-1} and ~5500 cm^{-1}, improving the overall outline of the calculated spectrum to some extent, but mismatch in band maxima remains between the experimental and the calculated spectra, along with discrepancies in the intensity distribution.

Three conspicuous neighboring peaks are observed in the lower frequency region of $MeOH_2^+\cdots(CO)_2$. For the peak at 4513 cm^{-1}, a similar band is observed in the other two spectra of the $n = 2$ clusters with an almost unchanged frequency. It can be found at ~4520 cm^{-1} also in the spectra of the $n = 1$ clusters. The same situation holds for the peak at 4233 cm^{-1}. These bands likely originate from the same vibrational source, suggesting a link to the CH vibrational motions excluded in the present calculations, given their consistent frequency and absence in every calculated spectrum. On the other hand, a pronounced peak is observed at 4391 cm^{-1}, to which corresponding bands are missing in the other $n = 2$ spectra. Though this band seems to be assigned to $|b + s\rangle$ because this CB is expected to be a major band in this region, this assignment cannot be reliable. Theoretically, the $|b$

View Article Online
DOI: 10.1039/D6CP00987E

$+ s\rangle$ transition should undergo coupling mechanisms resembling the situation in $MeOH_2^+\cdots CO$ with the dark states, which would lead to an appreciable broadening and redistribution of intensity rather than a narrow, well-isolated feature. Instead, this band may be attributed to the CB of the symmetric and antisymmetric C≡O stretches, which is reproduced at 4412 cm^{-1} by the DVR-FBR simulation. The $|b + s\rangle$ transition likely contributes to the broad background enveloping the prominent peaks around 4400 cm^{-1}.

Spectral broadening

Overall, both the NIR spectra reported here and the MIR spectra reported earlier [31] of $MeOH_2^+\cdots X_n$ exhibit significant spectral broadening. The extent of broadening tends to become more remarkable as the PA of the binding solvents increases. To examine whether thermal effects contribute to this broadening, we focused on the $MeOH_2^+\cdots(CO)_n$ clusters, for which the broadening effects are most pronounced.

The internal energy of a cluster is capped by the weakest intermolecular interaction in the cluster (here, the hydrogen bond), because clusters with internal energy surpassing this limit would undergo spontaneous dissociation before the spectroscopic measurement. We therefore compare the spectra of “bare” and Ar-“tagged” CO-solvated clusters. The additional Ar atom introduces a much weaker intermolecular bond, thereby limiting their internal energy. However, as the weakly-tagged clusters are thermodynamically unstable, the signal intensity of the parent ions is greatly reduced. This makes a direct comparison in the NIR region practically difficult. Instead, we compare the spectra in the MIR region by assuming their broadening mechanisms are similar to that of the NIR region.

Figures 3a and **3b** present the MIR spectra of $MeOH_2^+\cdots CO$ and $MeOH_2^+\cdots(CO)_2$, whereas **Figures 3c** and **3d** display the spectra of their Ar-tagged counterparts. Ar-tagging (*i.e.*, cooling) in **Figure 3c** has substantially narrowed the linewidths in the H-bonded OH

View Article Online
DOI: 10.1039/D6CP00987E

stretching region (2500-3000 cm^{-1}) for the $MeOH_2^+\cdots CO$ spectrum, supporting an inhomogeneous contribution to the broadening, that is expected to also influence the NIR region. In contrast, the lack of such narrowing for the "free" OH stretching bands at ~3400 cm^{-1} and ~3600 cm^{-1} (noted that in the Ar-tagged $MeOH_2^+\cdots(CO)$ cluster, the Ar atom binds to the free OH site, causing a red-shift of the band from ~3600 cm^{-1} to ~3400 cm^{-1}); these modes are less sensitive to the cooling in this situation. On the other hand, the cooling effect on $MeOH_2^+\cdots(CO)_2$ in **Figure 3d** is less significant across the entire spectral range, suggesting a smaller contribution of inhomogeneous broadening in the NIR region for this cluster.

An alternative source for the spectral broadening is the highly coupled low frequency vibrational modes such as t, R, and s_X modes. These modes can give rise to not only additional bands, but they also serve as pathways for IVR-based homogeneous broadenings. Here, the s_X and R modes, which have relatively higher frequencies, are isoenergetic with the OH stretching mode at several quanta; thus, these modes are expected to act as promoting modes in the IVR theory.[62] In contrast, the t mode, characterized by its extremely low frequency, functions as a typical bath mode.

The peak density distribution in the present NIR spectra of the protonated methanol clusters appears to be much higher in the 4000-5000 cm^{-1} region. As the solvent PA increases, the H-bonded OH stretching overtones gradually shift to this region where numerous minor states involving the low frequency modes are present. The further the $|s^2\rangle$ transition shifts toward this region, the more resonance/energy matching opportunities arise for couplings between $|s^2\rangle$ and other states. In extreme cases such as $MeOH_2^+\cdots CO$ and $MeOH_2^+\cdots(CO)_2$, the OH stretching overtone evolves into a strongly mixed manifold where mode-specific assignments are nearly inapplicable. Under such

View Article Online
DOI: 10.1039/D6CP00987E

circumstances, intensities of the bright states are severely diluted to form numerous "daughter" bands, ultimately leading to accelerated IVR and congested spectral profiles. In the regions near and below 5000 cm^{-1}, $|b+s\rangle$ is another major contributor to spectral broadening resembling the mechanisms of $|s^2\rangle$. State densities in the doubly solvated protonated methanol clusters are generally higher than those in the singly solvated ones due to the presence of an additional H-bonded solvent, which suggests even more of the above-mentioned coupling opportunities in the clusters with $n = 2$. However, there has been no strong evidence showing clear size dependence of spectral broadening at present. Such trends may be better viewed in solvated ammonium clusters in which the first solvation shell of the central cation may accommodate 4 solvent molecules.

Summary

We reported the NIR spectra of micro-solvated protonated methanol clusters in the region of the first OH stretching overtone. The H-bonded OH stretching overtones are significantly weaker than both the free OH stretching overtones and several pronounced CBs, which is consistent with the previously reported H-bonded systems. As the solvent species changes from Ar to CO (in the order of ascending solvent PA) at a fixed solvation number, the H-bonded OH stretching overtone bands become less intense, and a clear trend of spectral broadening was observed. The broadening can be attributed to a combination of hot band, IVR, and increased band congestion induced by numerous anharmonic couplings. Our reduce-dimensional DVR-FBR anharmonic analysis reproduces the overall spectral patterns of the NIR spectra. For the present system, our results also show the importance of explicitly including the relevant low-frequency modes, such as intermolecular H-bond stretching, CH bending, and solvent intramolecular

View Article Online
DOI: 10.1039/D6CP00987E

vibrations, since the overtone region is governed by extensive anharmonic mixings with these degrees of freedom.

Author contributions

Yaodi Yang: Investigation, Formal analysis, Data curation, Writing – original draft. Qian-Rui Huang: Methodology, Software, Formal analysis, Data curation, Writing – original draft. Jer-Lai Kuo: Conceptualization, Methodology, Supervision, Funding acquisition, Writing – review & editing. Asuka Fujii: Conceptualization, Methodology, Supervision, Funding acquisition, Writing – review & editing.

Conflicts of interest

There are no conflicts to declare.

Data availability

The data supporting this article are included in the supplementary information (SI). Supplementary information is available.

Acknowledgements

This study is supported by a Grant-in-Aid for Scientific Research (Project No. 21H04671 and 25K03402) from JSPS. Y. Y was supported by the AGS RISE program of Tohoku

View Article Online
DOI: 10.1039/D6CP00987E

University. Q.-R. H. and J.-L. K are supported by National Science and Technology Council, Taiwan (113-2113-M-001-032-MY3 and 114-2639-M-A49-002-ASP).

References

1 D. Boyall and K. L. Reid, Modern Studies of Intramolecular Vibrational Energy Redistribution, *Chem. Soc. Rev.*, 1997, **26**, 223–232.

2 H. Siesler, Y. Ozaki, S. Kawata and H. Heise, *Near-Infrared Spectroscopy: Principles, Instruments, Applications*, John Wiley & Sons, Inc., 2002.

3 C. Pasquini, Near Infrared Spectroscopy: Fundamentals, Practical Aspects and Analytical Applications, *J. Braz. Chem. Soc.*, 2003, **14**, 198–219.

4 K. B. Beć and C. W. Huck, Breakthrough Potential in Near-Infrared Spectroscopy: Spectra Simulation. A Review of Recent Developments, *Front. Chem.*, 2019, **7**, 48.

5 Y. Ozaki, Recent Advances in Molecular Spectroscopy of Electronic and Vibrational Transitions in Condensed Phase and Its Application to Chemistry, *Bull. Chem. Soc. Jpn.*, 2019, **92**, 629–654.

6 K. B. Beć, J. Grabska and Y. Ozaki, in *Frontiers of Quantum Chemistry*, eds. M. J. Wójcik, H. Nakatsuji, B. Kirtman and Y. Ozaki, Springer, Singapore, 2018, pp. 483–512.

7 P. Atkins, J. de Paula and J. Keeler, *Atkins' Physical Chemistry*, Oxford University Press, New York, 11th edn., 2018.

8 Y. Ozaki, C. Huck, S. Tsuchikawa and S. B. Engelsen, eds., *Near-Infrared Spectroscopy: Theory, Spectral Analysis, Instrumentation, and Applications*, Springer Nature, Singapore, 2020.

9 T. Ebata and M. Fujii, *Physical Chemistry of Cold Gas-Phase Functional Molecules and Clusters*, Springer, Singapore, 1st edn., 2019.

10 K. B. Beć, J. Grabska and C. W. Huck, Current and Future Research Directions in Computer-Aided Near-Infrared Spectroscopy: A Perspective, *Spectrochim. Acta A: Mol. Biomol. Spectrosc.*, 2021, **254**, 119625–119635.

View Article Online
DOI: 10.1039/D6CP00987E

11 M. Park, I. Shin, N. J. Singh and K. S. Kim, Eigen and Zundel Forms of Small Protonated Water Clusters: Structures and Infrared Spectra, *J. Phys. Chem. A*, 2007, **111**, 10692–10702.

12 M. Torrent-Sucarrat and J. M. Anglada, Anharmonicity and the Eigen-Zundel Dilemma in the IR Spectrum of the Protonated 21 Water Cluster, *J. Chem. Theor. Comput.*, 2011, **7**, 467–472.

13 C. T. Wolke, J. A. Fournier, L. C. Dzugan, M. R. Fagiani, T. T. Odbadrakh, H. Knorke, K. D. Jordan, A. B. McCoy, K. R. Asmis and M. A. Johnson, Spectroscopic Snapshots of the Proton-Transfer Mechanism in Water, *Science (1979).*, 2016, **354**, 1131–1135.

14 M. R. Fagiani, H. Knorke, T. K. Esser, N. Heine, C. T. Wolke, S. Gewinner, W. Schöllkopf, M.-P. Gaigeot, R. Spezia, M. A. Johnson and K. R. Asmis, Gas Phase Vibrational Spectroscopy of the Protonated Water Pentamer: The Role of Isomers and Nuclear Quantum Effects, *Phys. Chem. Chem. Phys.*, 2016, **18**, 26743–26754.

15 K. Yagi and B. Thomsen, Infrared Spectra of Protonated Water Clusters, $H^+(H_2O)_4$, in Eigen and Zundel Forms Studied by Vibrational Quasi-Degenerate Perturbation Theory, *J. Phys. Chem. A*, 2017, **121**, 2386–2398.

16 H. Wang and N. Agmon, Reinvestigation of the Infrared Spectrum of the Gas-Phase Protonated Water Tetramer, *J. Phys. Chem. A*, 2017, **121**, 3056–3070.

17 Q.-R. Huang, T. Nishigori, M. Katada, A. Fujii and J.-L. Kuo, Fermi Resonance in Solvated H_3O^+: A Counter-Intuitive Trend Confirmed *via* a Joint Experimental and Theoretical Investigation, *Phys. Chem. Chem. Phys.*, 2018, **20**, 13836–13844.

18 Q.-R. Huang, Y.-C. Li, T. Nishigori, M. Katada, A. Fujii and J.-L. Kuo, Vibrational Coupling in Solvated H_3O^+: Interplay between Fermi Resonance and Combination Band, *J. Phys. Chem. Lett.*, 2020, **11**, 10067–10072.

19 Y. Zhang, Y. Wang, X. Xu, Z. Chen and Y. Yang, Vibrational Spectra of Highly Anharmonic Water Clusters: Molecular Dynamics and Harmonic Analysis Revisited with Constrained Nuclear-Electronic Orbital Methods, *J. Chem. Theor. Comput.*, 2023, **19**, 9358–9368.

20 K. R. Asmis, Y. Yang, G. Santambrogio, M. Brümmer, J. R. Roscioli, L. R. McCunn, M. A. Johnson and O. Kühn, Gas-Phase Infrared Spectroscopy and Multidimensional Quantum Calculations of the Protonated Ammonia Dimer $N_2H_7^+$,

View Article Online
DOI: 10.1039/D6CP00987E

Angew. Chem. Int. Ed., 2007, **46**, 8691–8694.

21 Y. Yang, O. Kühn, G. Santambrogio, D. J. Goebbert and K. R. Asmis, Vibrational Signatures of Hydrogen Bonding in the Protonated Ammonia Clusters $NH_4^+(NH_3)_{1-4}$, *J. Chem. Phys.*, 2008, **129**, 224302–224308.

22 H. Wang and N. Agmon, Complete Assignment of the Infrared Spectrum of the Gas-Phase Protonated Ammonia Dimer, *J. Phys. Chem. A*, 2016, **120**, 3117–3135.

23 C.-K. Lin, Q.-R. Huang and J.-L. Kuo, Anharmonic Coupling behind Vibrational Spectra of Solvated Ammonium: Lighting up Overtone States by Fermi Resonance through Tuning Solvation Environments, *Phys. Chem. Chem. Phys.*, 2020, **22**, 24059–24069.

24 C.-K. Lin and J.-L. Kuo, Anharmonic IR Spectra of Solvated Ammonium and Aminium Ions: Resemblance between Water and Bisulfate Solvations, *Phys. Chem. Chem. Phys.*, 2022, **24**, 20318–20325.

25 R. Shishido, J.-L. Kuo and A. Fujii, Structures and Dissociation Channels of Protonated Mixed Clusters around a Small Magic Number: Infrared Spectroscopy of $((CH_3)_3N)_n$–H^+–H_2O (n = 1–3), *J. Phys. Chem. A*, 2012, **116**, 6740–6749.

26 M. Schütz, A. Bouchet and O. Dopfer, Infrared Spectrum of the Cold Ortho-Fluorinated Protonated Neurotransmitter 2-Phenylethylamine: Competition between $NH^+\cdots\pi$ and $NH^+\cdots F$ interactions, *Phys. Chem. Chem. Phys.*, 2016, **18**, 26980–26989.

27 C.-K. Lin, R. Shishido, Q.-R. Huang, A. Fujii and J.-L. Kuo, Vibrational Spectroscopy of Protonated Amine–Water Clusters: Tuning Fermi Resonance and Lighting up Dark States, *Phys. Chem. Chem. Phys.*, 2020, **22**, 22035–22046.

28 C.-K. Lin, Q.-R. Huang, M. Hayashi and J.-L. Kuo, An *Ab Initio* Anharmonic Approach to IR, Raman and SFG Spectra of the Solvated Methylammonium Ion, *Phys. Chem. Chem. Phys.*, 2021, **23**, 25736–25747.

29 J. R. Roscioli, L. R. McCunn and M. A. Johnson, Quantum Structure of the Intermolecular Proton Bond, *Science (1979).*, 2007, **316**, 249–254.

30 J. A. Tan and J.-L. Kuo, Strong Quantum Coupling in the Vibrational Signatures of a Symmetric Ionic Hydrogen Bond: The Case of $(CH_3OH)_2H^+$, *J. Phys. Chem. A*, 2015, **119**, 11320–11328.

View Article Online
DOI: 10.1039/D6CP00987E

31 C.-K. Lin, Q.-R. Huang, Y.-C. Li, H.-Q. Nguyen, J.-L. Kuo and A. Fujii, Anharmonic Coupling Revealed by the Vibrational Spectra of Solvated Protonated Methanol: Fermi Resonance, Combination Bands, and Isotope Effect, *J. Phys. Chem. A*, 2021, **125**, 1910–1918.

32 D. L. Howard and H. G. Kjaergaard, Influence of Intramolecular Hydrogen Bond Strength on OH-Stretching Overtones, *J. Phys. Chem. A*, 2006, **110**, 10245–10250.

33 C. -C. Wu, C. Chaudhuri, J. C. Jiang, Y. T. Lee and H. -C. Chang, On the First Overtone Spectra of Protonated Water Clusters [$H^+(H_2O)_{3–5}$] in the Free-OH Stretch Region, *J. Chin. Chem. Soc.*, 2002, **49**, 769–775.

34 J. P. Wagner, D. C. McDonald and M. A. Duncan, Near-Infrared Spectroscopy and Anharmonic Theory of the $H_2O^+Ar_{1,2}$ Cation Complexes, *J. Chem. Phys.*, 2017, **147**, 104302–104307.

35 D. C. McDonald, J. P. Wagner, A. B. McCoy and M. A. Duncan, Near-Infrared Spectroscopy and Anharmonic Theory of Protonated Water Clusters: Higher Elevations in the Hydrogen Bonding Landscape, *J. Phys. Chem. Lett.*, 2018, **9**, 5664–5671.

36 C. Schleif, H. A. Bunn, M. Jiménez-Redondo, P. Caselli and P. Jusko, Near-Infrared High Resolution Overtone Spectroscopy of the Hydronium Ion H_3O^+: The $2\nu_3^{2+}$ and $2\nu_3^{2-}$ Bands, *Phys. Chem. Chem. Phys.*, 2025, **27**, 21307–21314.

37 Q.-R. Huang, K. Yano, Y. Yang, A. Fujii and J.-L. Kuo, Near-Infrared Spectroscopy of $H_3O^+\cdots X_n$ (X = Ar, N_2, and CO, *n* = 1–3), *Phys. Chem. Chem. Phys.*, 2024, **26**, 10757–10768.

38 F. Kollipost, K. Papendorf, Y.-F. Lee, Y.-P. Lee and M. A. Suhm, Alcohol Dimers – How Much Diagonal OH Anharmonicity?, *Phys. Chem. Chem. Phys.*, 2014, **16**, 15948–15956.

39 H. G. Kjaergaard, E. Vogt, A. S. Bogomolov and C. Lauzin, The Elusive Bound OH-Stretching First Overtone of Water Dimer, *J. Phys. Chem. A*, 2026, **130**, 845–851.

40 P. Schuster, G. Zundel and C. Sandorfy, *The Hydrogen Bond: Recent Developments in Theory and Experiments*, North-Holland Pub. Co., Amsterdam, 1976.

41 J. M. Headrick, J. C. Bopp and M. A. Johnson, Predissociation Spectroscopy of

View Article Online
DOI: 10.1039/D6CP00987E

the Argon-Solvated $H_5O_2^+$ "Zundel" Cation in the 1000–1900 cm^{-1} Region, *J. Chem. Phys.*, 2004, **121**, 11523–11526.

42 U. Even, The Even-Lavie Valve as a Source for High Intensity Supersonic Beam, *EPJ Tech. Instrum.*, 2015, **2**, 17.

43 K. Mizuse and A. Fujii, Infrared Photodissociation Spectroscopy of $H^+(H_2O)_6 \cdot M_m$ (M = Ne, Ar, Kr, Xe, H_2, N_2, and CH_4): Messenger-Dependent Balance between H_3O^+ and $H_5O_2^+$ Core Isomers, *Phys. Chem. Chem. Phys.*, 2011, **13**, 7129–7135.

44 M. J. Frisch, G. W. Trucks, H. B. Schlegel, G. E. Scuseria, M. A. Robb, J. R. Cheeseman, G. Scalmani, V. Barone, G. A. Petersson, H. Nakatsuji, X. Li, M. Caricato, A. V Marenich, J. Bloino, B. G. Janesko, R. Gomperts, B. Mennucci, H. P. Hratchian, J. V Ortiz, A. F. Izmaylov, J. L. Sonnenberg, Williams, F. Ding, F. Lipparini, F. Egidi, J. Goings, B. Peng, A. Petrone, T. Henderson, D. Ranasinghe, V. G. Zakrzewski, J. Gao, N. Rega, G. Zheng, W. Liang, M. Hada, M. Ehara, K. Toyota, R. Fukuda, J. Hasegawa, M. Ishida, T. Nakajima, Y. Honda, O. Kitao, H. Nakai, T. Vreven, K. Throssell, J. A. Montgomery Jr., J. E. Peralta, F. Ogliaro, M. J. Bearpark, J. J. Heyd, E. N. Brothers, K. N. Kudin, V. N. Staroverov, T. A. Keith, R. Kobayashi, J. Normand, K. Raghavachari, A. P. Rendell, J. C. Burant, S. S. Iyengar, J. Tomasi, M. Cossi, J. M. Millam, M. Klene, C. Adamo, R. Cammi, J. W. Ochterski, R. L. Martin, K. Morokuma, O. Farkas, J. B. Foresman and D. J. Fox, *Gaussian 16, Revision C.01*, Gaussian, Inc., Wallingford, CT, 2016.

45 J. D. Head, Computation of Vibrational Frequencies for Adsorbates on Surfaces, *Int. J. Quantum Chem.*, 1997, **65**, 827–838.

46 Q.-R. Huang, Y.-C. Li, K.-L. Ho and J.-L. Kuo, Vibrational Spectra of Small Methylamine Clusters Accessed by an *ab initio* Anharmonic Approach, *Phys. Chem. Chem. Phys.*, 2018, **20**, 7653–7660.

47 Q. Huang, R. Shishido, C. Lin, C. Tsai, J. A. Tan, A. Fujii and J. Kuo, Strong Fermi Resonance Associated with Proton Motions Revealed by Vibrational Spectra of Asymmetric Proton-Bound Dimers, *Angew. Chem. Int. Ed.*, 2021, **60**, 1936–1941.

48 J. C. Light and T. Carrington, in *Advances in Chemical Physics*, eds. I. Prigogine and S. A. Rice, John Wiley & Sons, Inc., 2000, vol. 114, pp. 263–310.

49 B. Shizgal, *Spectral Methods in Chemistry and Physics*, Springer Netherlands, Dordrecht, 2015.

View Article Online
DOI: 10.1039/D6CP00987E

50 S. Carter, J. M. Bowman and N. C. Handy, Extensions and Tests of 'Multimode': A Code to Obtain Accurate Vibration/Rotation Energies of Many-Mode Molecules, *Theor. Chem. Acc.*, 1998, **100**, 191–198.

51 F. Neese, Software Update: The ORCA Program System—Version 6.0, *WIREs Comput. Mol. Sci.*, 2025, **15**, e70019.

52 *Intel® oneAPI Math Kernel Library*, *ver. 2022.0.2*, Intel Corporation, Santa Clara, CA, 2022.

53 G. W. Stewart, A Krylov-Schur Algorithm for Large Eigenproblems, *SIAM J. Matrix Anal. Appl.*, 2002, **23**, 601–614.

54 G. E. Hilbert, O. R. Wulf, S. B. Hendricks and U. Liddel, A Spectroscopic Method for Detecting some Forms of Chelation, *Nature*, 1935, **135**, 147–148.

55 G. E. Hilbert, O. R. Wulf, S. B. Hendricks and U. Liddel, The Hydrogen Bond between Oxygen Atoms in Some Organic Compounds, *J. Am. Chem. Soc.*, 1936, **58**, 548–555.

56 A. Foldes and C. Sandorfy, Anharmonicity and Hydrogen Bonding: Part III. Examples of Strong Bonds. General Discussion, *J. Mol. Spectrosc.*, 1966, **20**, 262–275.

57 T. Di Paolo, C. Bourdéron and C. Sandorfy, Model Calculations on the Influence of Mechanical and Electrical Anharmonicity on Infrared Intensities: Relation to Hydrogen Bonding, *Can. J. Chem.*, 1972, **50**, 3161–3166.

58 T. Gonjo, Y. Futami, Y. Morisawa, M. J. Wojcik and Y. Ozaki, Hydrogen Bonding Effects on the Wavenumbers and Absorption Intensities of the OH Fundamental and the First, Second, and Third Overtones of Phenol and 2,6-Dihalogenated Phenols Studied by Visible/Near-Infrared/Infrared Spectroscopy, *J. Phys. Chem. A*, 2011, **115**, 9845–9853.

59 Y.-L. Cheng, H.-Y. Chen and K. Takahashi, Theoretical Calculation of the OH Vibrational Overtone Spectra of 1-*n* Alkane Diols (n = 2–4): Origin of Disappearing Hydrogen-Bonded OH Peak, *J. Phys. Chem. A*, 2011, **115**, 5641–5653.

60 E. P. L. Hunter and S. G. Lias, Evaluated Gas Phase Basicities and Proton Affinities of Molecules: An Update, *J. Phys. Chem. Ref. Data*, 1998, **27**, 413–656.

View Article Online
DOI: 10.1039/D6CP00987E

61 D. Bing, T. Hamashima, A. Fujii and J.-L. Kuo, Anticooperative Effect Induced by Mixed Solvation in $H^+(CH_3OH)_m(H_2O)_n$ ($m + n = 5$ and 6): A Theoretical and Infrared Spectroscopic Study, *J. Phys. Chem. A*, 2010, **114**, 8170–8177.

62 J. Jortner, S. A. Rice and R. M. Hochostrasser, in *Advances in Photochemistry*, eds. J. N. Pitts, G. S. Hammond and W. A. Noyes, John Wiley & Sons, Inc., 1969, vol. 7, pp. 149-309.

View Article Online
DOI: 10.1039/D6CP00987E

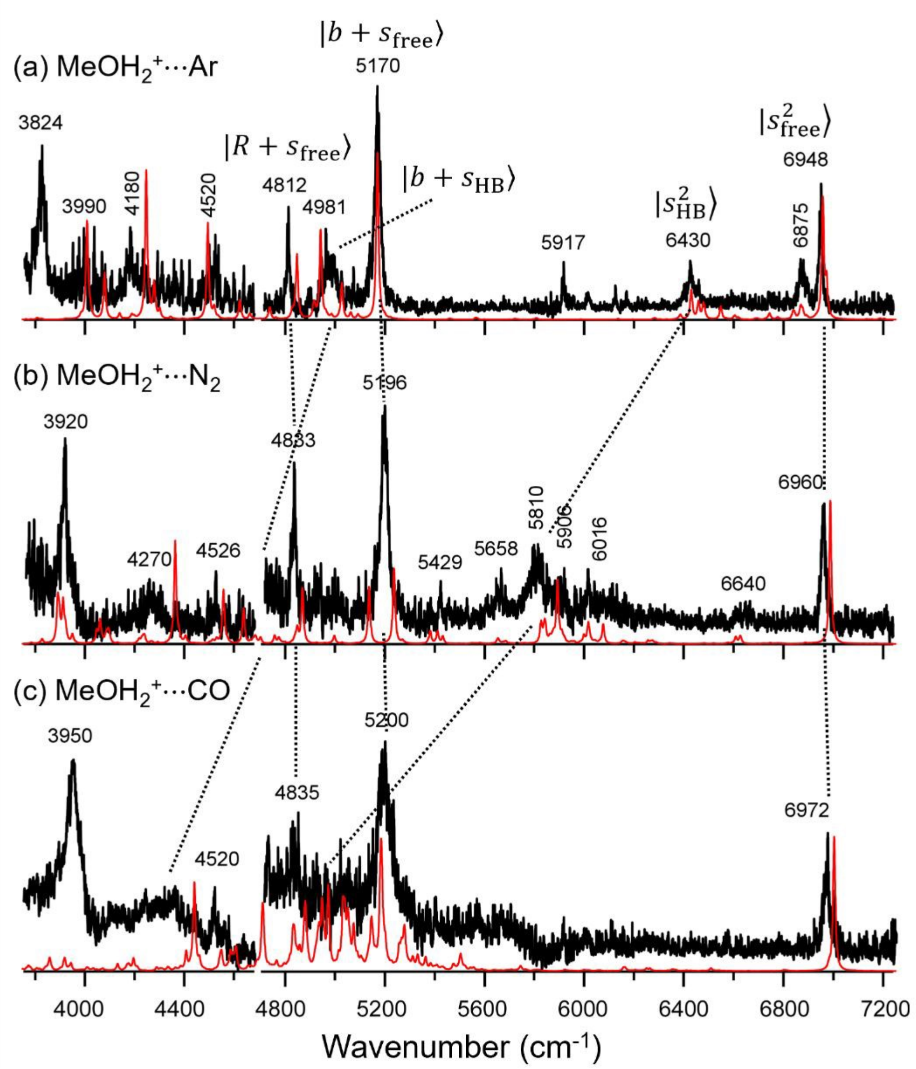

Figure 1. Observed (black) and calculated (red) NIR spectra of $MeOH_2^+\cdots X$, (a) X = Ar, (b) X = N_2, and (c) X = CO. Each observed spectrum was obtained by monitoring its one-solvent-loss dissociation channel. All numbers labeled on the spectra are observed band frequencies.

View Article Online
DOI: 10.1039/D6CP00987E

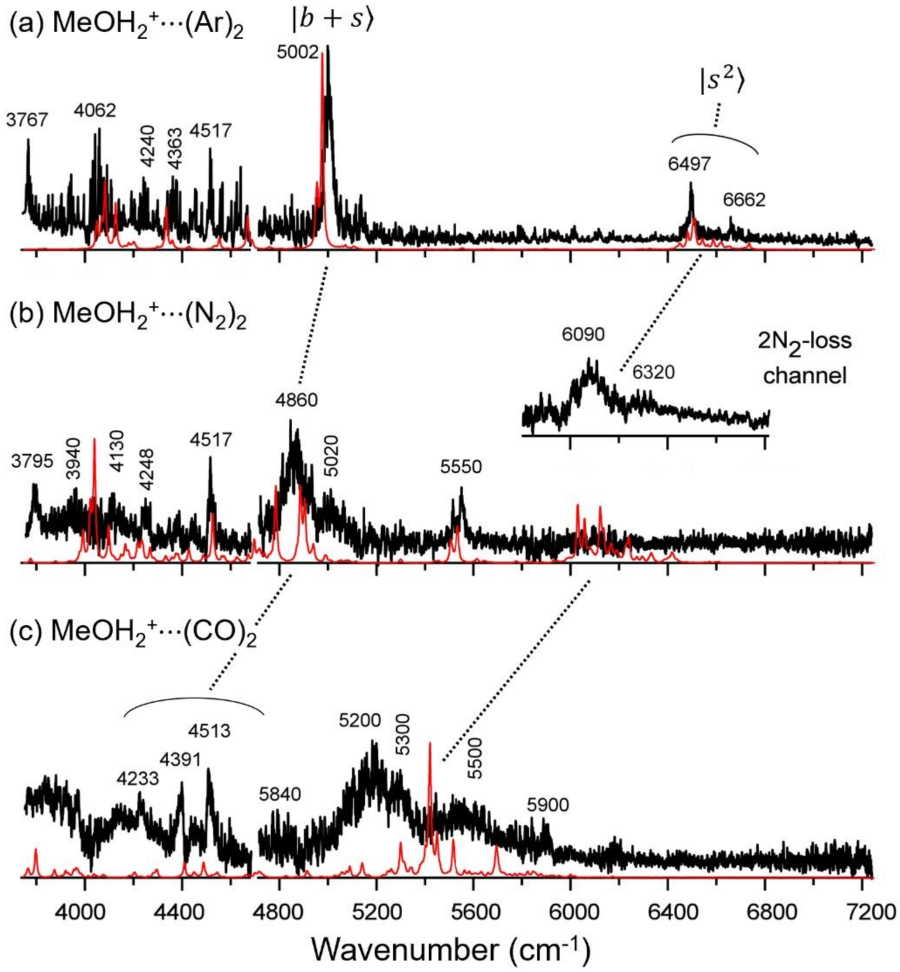

Figure 2. Observed (black) and calculated (red) NIR spectra of $MeOH_2^+\cdots(X)_2$. (a) X = Ar. The observed spectrum was obtained by monitoring the 2Ar-loss dissociation channel. (b) X = N_2. The main spectrum was obtained by monitoring the N_2-loss dissociation channel. The inset shows the spectrum obtained by monitoring the $2N_2$-loss dissociation channel. (c) X = CO. The spectrum was obtained by monitoring the CO-loss dissociation channel. All numbers are observed band frequencies.

View Article Online
DOI: 10.1039/D6CP00987E

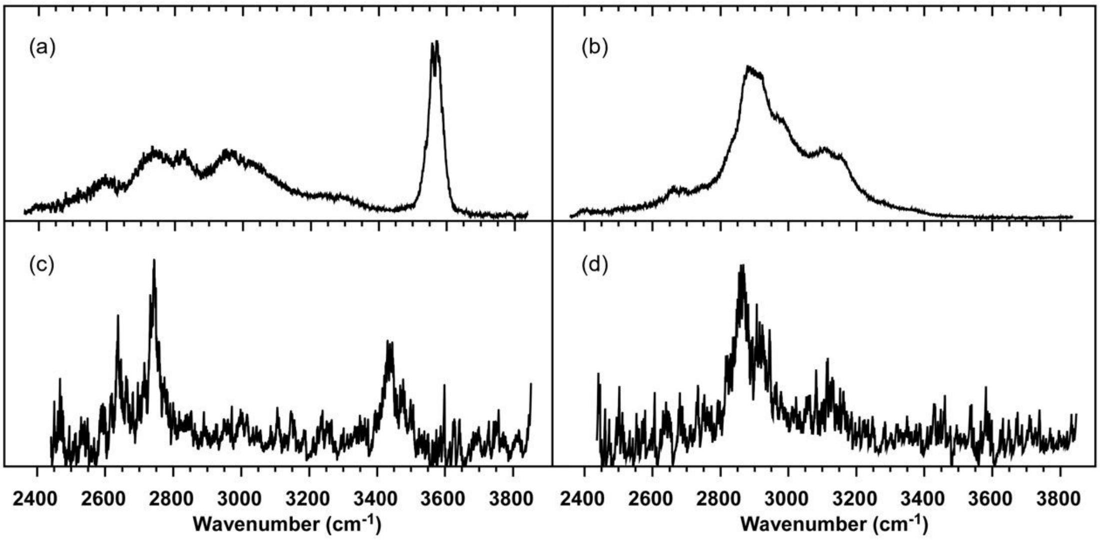

Figure 3. Experimental IRPD spectra of (a) $MeOH_2^+\cdots CO$, (b) $MeOH_2^+\cdots(CO)_2$, (c) $MeOH_2^+\cdots CO\cdots Ar$, and (d) $MeOH_2^+\cdots(CO)_2\cdots Ar$ in the MIR region.

View Article Online
DOI: 10.1039/D6CP00987E

Data availability statements

The data supporting this article have been included as part of the Supplementary Information.